Dynamic Fracture Characterization of Small Specimens: A Study of Loading Rate Effects on Acrylic and Acrylic Bone Cement

Robert Bedsole

Hareesh V. Tippur
e-mail: tippuhv@auburn.edu

Department of Mechanical Engineering,
Auburn University,
Auburn, AL 36849

A long-bar apparatus for subjecting relatively small samples to stress-wave loading has been devised for failure characterization. A methodology based on digital image correlation (DIC) used in conjunction with ultra high-speed photography and a long-bar impactor has been developed for determining dynamic crack initiation stress intensity factor (SIF) (K_{I-ini}^d), as well as SIFs for a rapidly growing crack (K_I^d) during high-strain rate events. By altering the material of the pulse shaper, a range of strain rates has been attained. Commercial grade PMMA was first used to calibrate the device, and then dynamic fracture characterization was performed for the first time on PMMA-based bone cement (BC). Despite several key differences, the two materials performed similarly during quasi-static fracture tests; however, under dynamic loading conditions, bone cement exhibited significantly lower crack initiation SIF (K_{I-ini}^d), lower dynamic SIFs (K_I^d), and higher crack tip velocities for three different dynamic loading rates $(\dot{K} = 6.5 - 24 \times 10^4\, MPa\sqrt{m}\,s^{-1})$. [DOI: 10.1115/1.4023405]

Keywords: fracture, strain-rate effects, digital image correlation, split-Hopkinson bar, PMMA, bone cement

Introduction

In 1960, Charnley began anchoring femoral head prostheses with acrylic cement in order to improve the load distribution between implant and femur. Instead of high adhesive properties or mechanical strength, this solution offered a "tailored" fit to the bone that previous metal-only implants could not achieve [1]. Charnley's method is still widely used [2], although uncemented techniques have also been developed in which the surrounding bone grows directly into the roughened surface of the implant. These newer uncemented prostheses are designed primarily for younger patients and have not been as consistently successful as cemented implants [3].

Due to the poor adhesive properties of acrylic (PMMA) bone cement, corresponding implant designs include holes, grooves, and other geometric features for mechanical interlocking between implant and cement. The roughened bone surface (due to reaming) then ensures mechanical interlock between cement and bone. Over time, these interfaces can deteriorate, eventually leading to revision surgeries [4]. Additional problems associated with cemented prosthesis interfaces include necrosis of surrounding bone tissue due to exothermic polymerization [2,4,5], stress concentrations due to nonuniform temperature distribution during cooling [2], shrinkage of the cement mantle during hardening [2,4,5], and potential release of toxic monomer. Any untreated MMA monomer is a toxic fat solvent [2] and may result in allergic reaction and an unsafe drop in blood pressure [5], as well as locally interfering with postoperative healing [2].

In addition to the cement-implant and cement-bone interfaces, the cement mantle itself has been implicated as the site of

initiation of implant failure [6,7]. Pore formation in the cement mantle is unavoidable [8] and has been the origin of fracture in vivo [6,7]. While Jasty et al. [8] showed some improvement in the bulk porosity of certain bone cements through the usage of centrifugation, voids could not be eliminated completely. Such cracks that initiate and propagate within the cement mantle will be the focus of the present work.

The quasi-static crack initiation SIF (K_{IC}) of acrylic bone cement is well documented in the literature (Table 1). This value characterizes the ability of a material to resist crack growth. However, to date, the authors are unaware of reports on dynamic fracture properties of bone cement, either at crack initiation or during crack propagation. This gap needs to be bridged because failure of the implant could initiate in the cement mantle under impact or shock loading events such as jumping, falling, tackling, and auto accidents. More active patients considered most likely to experience these types of loading events are typically given uncemented prostheses; this tendency will likely be supported in this work after quantifying the dynamic fracture response of bone cement. Additionally, whether unstable crack growth within the cement

Table 1 The quasi-static crack initiation SIF (K_{IC}) of various clinical bone cements, including Cemex® with and without a radiopacifier

Type	$K_{IC}(MPa\sqrt{m})$	Radiopacifier	Author
CMW³	2.19	BaSO₄	Buckley et al. [9]
CMW³	2.22	BaSO₄	Ishihara et al. [10]
Súbiton gun	1.60	BaSO₄	Vallo et al. [11]
Súbiton 6'	1.33	BaSO₄	Vallo et al. [11]
Palacos R	1.78	ZrO₂	Vallo et al. [11]
Cemex	1.36	BaSO₄	Baleani and Viceconti [12]
Cemex	1.56	None	Baleani and Viceconti [12]

Table 2 The quasi-static crack initiation SIF values (K_{IC}) for PMMA determined by several research teams, along with the dynamic crack initiation SIF (K_{I-ini}^d) and corresponding dynamic loading rates ($\dot{K}$)

Quasi-static K_{IC}(MPa$\sqrt{\text{m}}$)	Dynamic loading rate $\dot{K}$(MPa$\sqrt{\text{m}}\,\text{s}^{-1}$)	Dynamic K_{I-ini}^d(MPa$\sqrt{\text{m}}$)	Author
1.2	—	—	Johnson and Jones [13]
2.2	4.52×10^4–2.10×10^5	2.17–6.15	Rittel and Maigre [14]
1.42–1.68	5×10^3–5×10^4	2.47–4.06	Weerasooriya et al. [15]
1.45–1.66	5.2×10^3–8.3×10^4	1.00–1.34	Wada [16]
—	0.7×10^4–9.0×10^4	0.28–3.68	Wada and Seika [17]

mantle is caused by a dynamic loading event or fatigue crack growth that gives way to sudden rapid crack growth, the resulting outcome is very similar; in both cases, it is important to assess the material's ability to arrest a rapidly growing crack. Therefore, the primary objective of this study is to determine the dynamic fracture properties of DePuy® CMW MV bone cement, both at crack initiation and during rapid crack propagation. Because the quasi-static properties of this bone cement have not been reported, both quasi-static crack initiation SIF (K_{IC}) and dynamic crack initiation SIF (K_{I-ini}^d) of this material will be determined. In order to calibrate the dynamic loading device, the same fracture tests will be carried out on commercial grade acrylic, as this material has been well documented in both quasi-static and dynamic fracture (Table 2).

The final objective of this study is to introduce a methodology for determining the dynamic fracture properties of relatively small size specimens (1 in. × 2 in. in this study). Planned research in the near future will also include the dynamic fracture characterization of cortical bone, which is difficult to obtain in large geometries. Many researchers offer techniques for finding dynamic crack initiation SIF, but few have developed methods for characterizing the material's ability to retard crack growth once it has begun. Both types of fracture data are crucial for evaluating the suitability of a particular bone cement under dynamic loading. Nam et al. [18] applied loading velocities of 1–7 m/s to metal-matrix composites (100 × 15 × 3 mm) using a falling dart fitted with a load cell in order to determine peak load at initiation and calculate initiation SIF. Martins et al. [19] used strain gages on a modified split-Hopkinson pressure bar with rigid supports for three-point bending in order to determine critical energy release rate of linear medium density polyethylene (50 × 10 × 10 mm). Weisbrod and Rittel [20] measured crack initiation SIF with a modified split-Hopkinson pressure bar that delivered one-point impact loading to short tungsten alloy specimens (23 × 10 × 8 mm) with strain gages placed both on the long-bar and on the specimen. None of the above methods addressed the resistance of the material to further crack growth once initiation had occurred.

Several teams have modified the split-Hopkinson pressure bar to measure fracture parameters on Brazilian disc specimens [21–24]. These researchers have used strain gages on the incident and transmission bars to determine the peak load, fracture gages on the specimen to monitor fracture, and laser gap gages to measure crack opening displacement. These techniques do not offer full-field information about crack initiation or growth characteristics. Also without a camera monitoring the position of the crack tip, SIFs measured after initiation could be unreliable, as these depend on the instantaneous crack tip velocity.

Shukla et al. [25] used a split-Hopkinson pressure bar modified for three-point bending tests, along with high-speed photography and photoelasticity, to find dynamic crack initiation SIF as a function of velocity in nanocomposites; however, the samples tested were much larger in size (280 × 150 mm and 254 × 240 mm). Lee et al. [26] used a low velocity falling dart, along with high-speed photography and digital image correlation (DIC), to find dynamic crack initiation SIF as a function of time for unidirectional composites (200 × 50 × 6.2 mm). The proposed methods involve higher velocity fracture tests with smaller specimens than Lee et al. [26] by utilizing a one-point impactor, high-speed photography (~300,000 frames per second), and DIC during crack

initiation and propagation. SIFs are extracted from two-dimensional data fields with approximately 400 data points on the specimen surface using DIC. The high-speed images are also used to locate the instantaneous crack tip, such that crack tip velocities can be estimated.

Specimen Preparation

There are several major differences between commercial grade acrylic sheets and the DePuy bone cement used in this study. Both polymerization reactions include prepolymerized PMMA beads, an initiator, and MMA monomer. However, commercial grade acrylic sheets are cured slowly (in about twelve hours) under high pressure and high temperature, while the DePuy bone cement is cured in less than 20 min at relatively low pressure and temperature in view of its intended use. Thus, the porosity of a bone cement will generally be higher than that of a commercial acrylic. Again, these bone cement pores are present both in the surgical theatre as well as in the laboratory experiments described below. Relatively large pores (~1 mm) are believed to be caused by air entrapment during mixing of the liquid phase with the powder phase, while smaller voids (~100 μm) are created by gaseous byproducts of the polymerization reaction [8]. In addition, the conditions of the industrial grade acrylic reaction lead to a homogenous dispersion of fully entangled PMMA chains, while the bone cement reaction creates a two-phase material: prepolymerized beads within an interbead matrix. The interbead matrix shrinks during polymerization, potentially causing shrinkage stresses between the two phases. The interbead matrix also contains the radiopacifier barium sulfate (BaSO$_4$) so that the bone cement mantle can be visualized on X-ray after surgery. Previous studies have shown that the addition of BaSO$_4$ to pure PMMA leads to a significant reduction in fatigue strength [27] and quasi-static crack initiation SIF [12] (Table 1). This is likely due to the poor bonding between BaSO$_4$ particles and the interbead matrix. Finally, a cross-linking agent has been added to this particular commercial grade acrylic, increasing its T_g from the typical value of 105 °C for PMMA to 122 °C. The T_g for bone cement was 101 °C (as measured by Differential Scanning Calorimetry).

Two specimen material types were used: commercial grade cast acrylic (hereon referred to as PMMA) purchased from McMaster Carr and DePuy® CMW SmartSet Endurance Medium Viscosity BC, prepared according to manufacturer instructions. The powder phase (10% by weight BaSO$_4$) of BC was combined with the liquid phase using a DePuy® vacuum mixer. After 90 s, the BC was poured onto a plate and allowed to cure for 20 min (Fig. 1). Due to the fast curing time, low temperature, and low pressure of medical grade bone cement, some degree of pore formation was
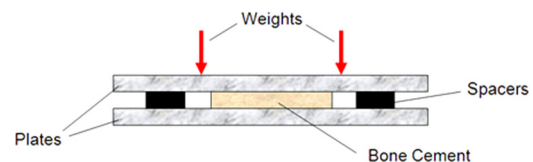
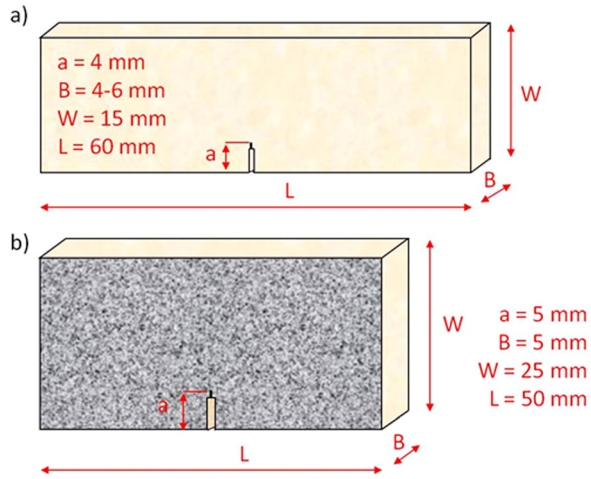**Fig. 1 Bone cement sheet cures between two plates using spacers for desired thickness**

Fig. 2 Static (*a*) and dynamic and (*b*) specimen geometry

unavoidable [8]. These voids typically rose to the surface and most were skimmed during processing or removed with a mill during sizing. However, some pores remained in the final BC specimens (estimated to be ~1% porosity by area measured on fracture surfaces), while PMMA specimens did not have these defects.

For the static three-point bending tests, PMMA and BC specimens were machined to beam shapes of $60 \times 15 \times 4$–$6\,mm$ (Fig. 2(*a*)). For the dynamic one-point impact tests, plate-shaped specimens of $50 \times 25 \times 5\,mm$ were used (Fig. 2(*b*)). The larger width of the dynamic specimens allowed for additional investigation of fracture parameters for the growing crack. All specimens were prenotched using a diamond tipped saw. A speckle coating was spray-painted onto dynamic specimens in order to monitor in-plane displacements using DIC (to be explained in the Experimental Analysis section).

Experimental Details

Quasi-Static Tests. PMMA and BC specimens were tested in symmetric three-point bending configuration using an Instron 4465 testing machine in displacement control mode (cross-head speed $= 0.01\,mm/s$). The samples were loaded monotonically up to fracture. The load-displacement responses were essentially linear up to crack initiation and fracture occurred abruptly during the tests. The quasi-static initiation SIFs (K_{IC}) were calculated based on the maximum recorded load using

$$K_{IC} = \frac{\left(\frac{P_{max}}{B\sqrt{W}}\right)\left(3\frac{S}{W}\sqrt{\frac{a}{W}}\right)}{2\left(1 + 2\frac{a}{W}\right)\left(1 - \frac{a}{W}\right)^{3/2}}$$
$$\times \left[1.99 - \frac{a}{W}\left(1 - \frac{a}{W}\right)\left\{2.15 - 3.93\left(\frac{a}{W}\right) + 2.7\left(\frac{a}{W}\right)^2\right\}\right] \quad (1)$$

where P_{max} is the peak load prior to fracture, B is thickness, W is width, S is span ($50.9\,mm$), and a is crack length.

Dynamic Tests

Experimental Setup. In order to study dynamic fracture of relatively small specimens, a methodology (Fig. 3) that employs DIC and high-speed photography to monitor in-plane deformations on a plate-shaped specimen during a one-point impact loading event has been developed. A striker is launched at approximately $16\,m/s$ from a compressed air chamber into a long-bar (incident bar) made of strain-rate independent Al 7075 T6. A pulse shaper is used between the striker and long-bar as needed in order to affect the loading rate. A strain gage on the long-bar records the incident stress wave, which is later used in a computational model for verification of the experimental results. The stress wave then enters the specimen via a semicircular head machined onto the end of the long-bar. The specimen rests on an adjustable stage (Fig. 4) without any constraints and thus experiences a simple one-point impact. The sample loading is symmetric with respect to the prenotch in order to achieve mode-I fracture. Symmetric loading conditions are further ensured by placing a layer of putty above and below the specimen. The stress wave enters the specimen as a compressive wave and reflects back as a tensile stress wave from the prenotched edge. Due to inertia, the reflected tensile waves subject the crack to mode I loading long before the specimen leaves the field of view of the high-speed camera.

Three different dynamic strain-rates were achieved through the usage of different pulse shapers (Fig. 5). A soft Aluminum 1100 disc (Al) of diameter $8\,mm$ and thickness $0.9\,mm$ produced a strain-rate of $10.7\,s^{-1}$, *measured on the long-bar*. A combined polycarbonate washer (outer diameter $6.3\,mm$, inner diameter $2.2\,mm$ and thickness $0.7\,mm$) and Al 1100 sandwich pulse shaper (Al/PC) produced a slightly lower strain rate of $3.7\,s^{-1}$. The highest strain rate was $42.0\,s^{-1}$ when no pulse shaper (none) was used.

Experimental Analysis. A Cordin model 550 high-speed digital camera was used for recording the dynamic fracture events at 200,000–400,000 frames per second. The camera has 32 CCD sensors and uses a high-speed rotating mirror to smear the image
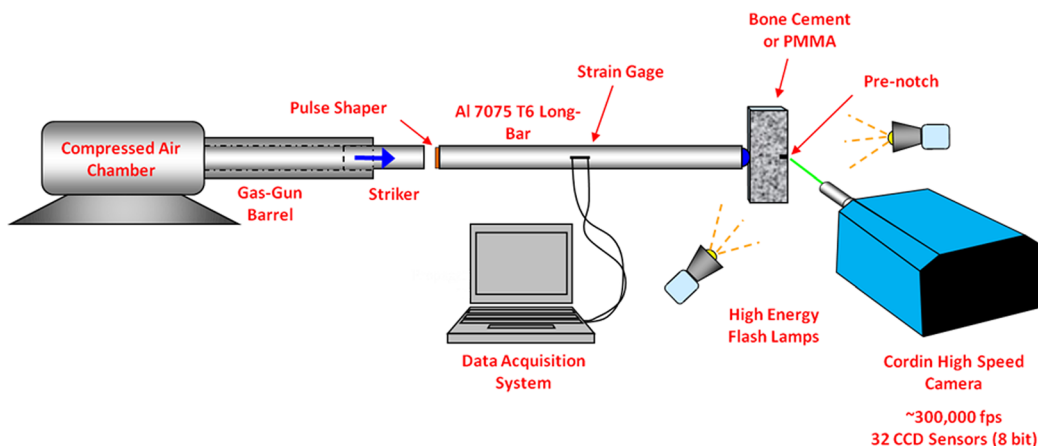

Fig. 3 Schematic of long-bar impactor setup for studying crack initiation and propagation of relatively small size specimens
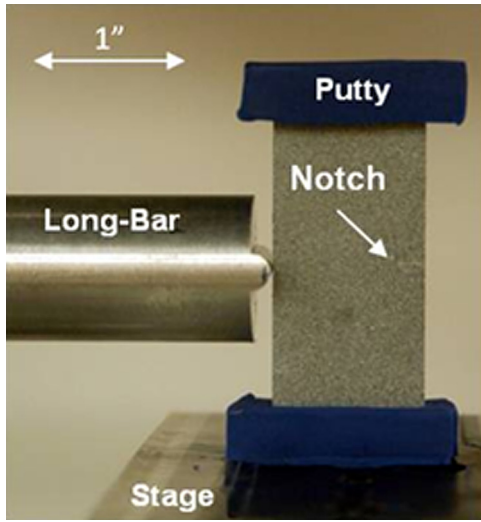
Fig. 4 Close-up of the impact loading setup. Specimen with prenotch is placed in contact with the semicircular impactor head of the long-bar prior to testing. Putty is used to ensure symmetry of reflected waves from the top and bottom specimen edges.

Fig. 6 (a) A pair of images recorded from the same CCD sensor of the high-speed camera. (b) Point O in the undeformed sub-image displaces to a location O' in the deformed subimage. The difference in these coordinates gives the sliding (u) and opening (v) displacements for the subimage.

over the sensors during the fracture event. Prior to each event, 32 undeformed images were recorded at the same framing rate as the deformed images. Undeformed and deformed images from the same sensor were matched (Fig. 6(a)), and 2D DIC was carried
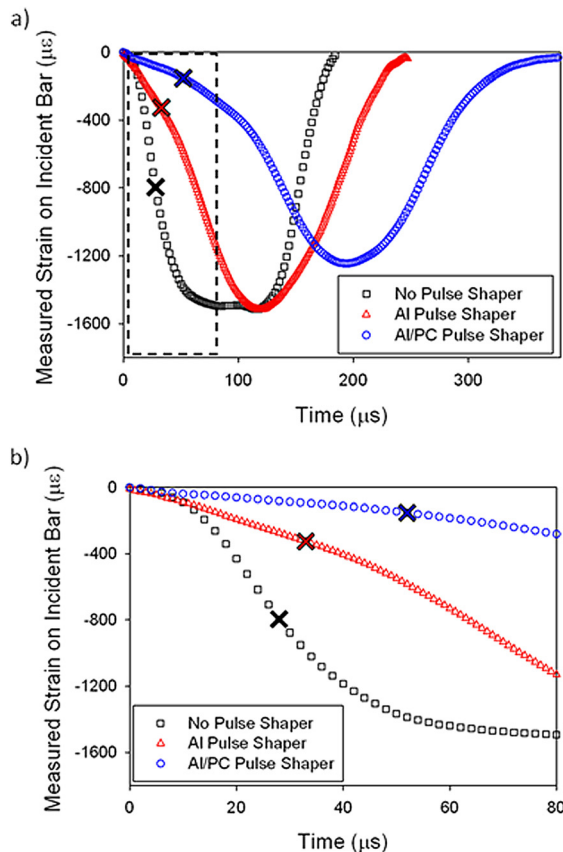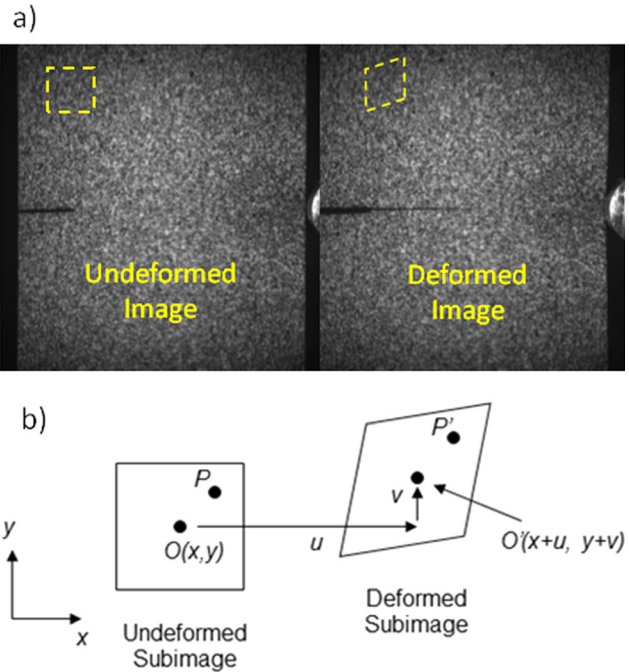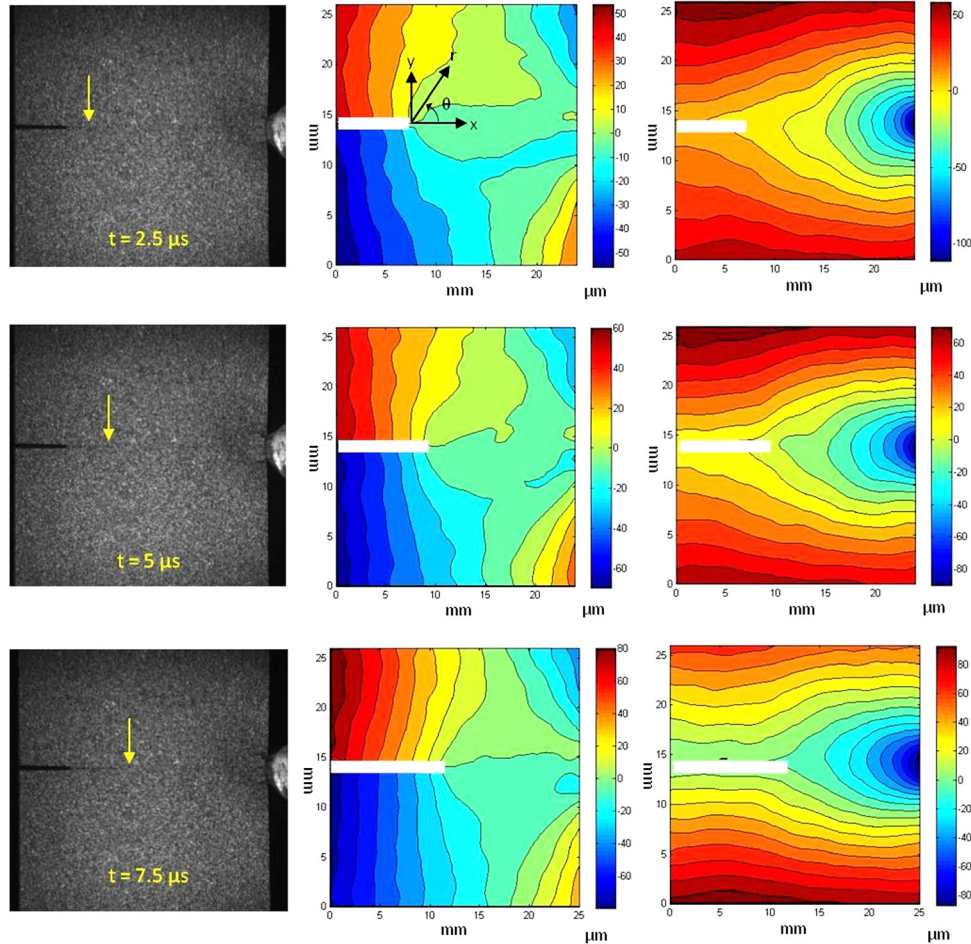

Fig. 5 (a) Strain histories *recorded on the long-bar* corresponding to three different pulse shapers. X marks the portion of the strain history coinciding with crack initiation. (b) The first 80 μs of Fig. 5(a) are shown.

out on each of the 32 image pairs using ARAMIS® software in order to determine in-plane displacement fields. Individual 1000×1000 pixel images were segmented into subimages of size 15×15 pixels. For a subimage identified in an undeformed image, the corresponding speckle pattern is searched in the deformed image. The center point of the matched undeformed subimage (O) and that of the deformed subimage (O') have coordinates (x,y) and ($x+u, y+v$), respectively, (Fig. 6(b)). By repeating this process for all subimages, a 66×66 matrix of in-plane displacements (u,v) were created for each image. Contour plots based of these matrices are shown in Figs. 7(b) and 7(c) corresponding to the deformed images in Fig. 7(a).

The crack tip location is identified for each deformed image and set to zero displacement. The u and v displacements for the region of interest are then interpolated from the original 66×66 matrix. This region ($0.5 < r/B < 1.5$ and $-150 \deg < \theta < -90 \deg$ or $90 \deg < \theta < 150 \deg$) was chosen to avoid 3D effects near the crack tip and far field effects on this relatively small specimen.

The SIFs were determined for each image prior to crack initiation using asymptotic expressions for displacements:

$$u(r,\theta) = \sum_{n=1}^{\infty} \frac{(K_I)_n}{2\mu} \frac{r^{n/2}}{\sqrt{2\pi}} \left\{ \kappa \cos\frac{n}{2}\theta - \frac{n}{2}\cos\left(\frac{n}{2}-2\right)\theta \right.$$
$$\left. + \left\{ \frac{n}{2}+(-1)^n \right\} \cos\frac{n}{2}\theta \right\} + \sum_{n=1}^{\infty} \frac{(K_{II})_n}{2\mu} \frac{r^{n/2}}{\sqrt{2\pi}}$$
$$\times \left\{ \kappa \sin\frac{n}{2}\theta - \frac{n}{2}\sin\left(\frac{n}{2}-2\right)\theta + \left\{ \frac{n}{2}-(-1)^n \right\} \sin\frac{n}{2}\theta \right\}$$
$$v(r,\theta) = \sum_{n=1}^{\infty} \frac{(K_I)_n}{2\mu} \frac{r^{n/2}}{\sqrt{2\pi}} \left\{ \kappa \sin\frac{n}{2}\theta + \frac{n}{2}\sin\left(\frac{n}{2}-2\right)\theta \right.$$
$$\left. - \left\{ \frac{n}{2}+(-1)^n \right\} \sin\frac{n}{2}\theta \right\} + \sum_{n=1}^{\infty} \frac{(K_{II})_n}{2\mu} \frac{r^{n/2}}{\sqrt{2\pi}}$$
$$\times \left\{ -\kappa \cos\frac{n}{2}\theta - \frac{n}{2}\cos\left(\frac{n}{2}-2\right)\theta + \left\{ \frac{n}{2}-(-1)^n \right\} \cos\frac{n}{2}\theta \right\}$$
$$(2)$$

Fig. 7 Images recorded of a crack growing in bone cement using an Al pulse shaper at 2.5, 5, and 7.5 μs after initiation. Corresponding crack opening (*b*) and sliding (*c*) displacement fields are shown. Contour interval is 10 μm. Symmetry of sliding displacements indicates Mode I dominant fracture. Arrows indicate crack tip location.

in the region of interest. Here, r and θ are the polar coordinates with origin at the crack tip, $(K_I)_1$ is the SIF associated with mode I fracture, $(K_{II})_1$ is the SIF associated with mode II fracture, μ is the shear modulus, υ is the Poisson's ratio, and $\kappa = (3 - \upsilon)/(1 + \upsilon)$ for plane stress. Because K_I is most closely associated with opening displacements and K_{II} is most closely associated with sliding displacements, least squares solutions for K_I were recorded from the v field, and K_{II} values were determined from the u field. Similarly, crack tip deformations described by Nishioka and Atluri's [28] equations (Eq. (3)) were employed for finding SIFs for the growing crack:

$$
u(r, \theta) = \sum_{n=1}^{\infty} \frac{(K_I)_n B_I(c)}{2\mu} \sqrt{\frac{2}{\pi}} (n+1) \left\{ r_1^{n/2} \cos \frac{n}{2} \theta_1 \right.
$$
$$
\left. - h(n) r_2^{n/2} \cos \frac{n}{2} \theta_2 \right\} + \sum_{n=1}^{\infty} \frac{(K_{II})_n B_{II}(c)}{2\mu} \sqrt{\frac{2}{\pi}} (n+1)
$$
$$
\times \left\{ r_1^{n/2} \sin \frac{n}{2} \theta_1 - h(\bar{n}) r_2^{n/2} \sin \frac{n}{2} \theta_2 \right\}
$$
$$
v(r, \theta) = \sum_{n=1}^{\infty} \frac{(K_I)_n B_I(c)}{2\mu} \sqrt{\frac{2}{\pi}} (n+1) \left\{ -\beta_1 r_1^{n/2} \sin \frac{n}{2} \theta_1 \right.
$$
$$
\left. - \frac{h(n)}{\beta_2} r_2^{n/2} \sin \frac{n}{2} \theta_2 \right\} + \sum_{n=1}^{\infty} \frac{(K_{II})_n B_{II}(c)}{2\mu} \sqrt{\frac{2}{\pi}} (n+1)
$$
$$
\times \left\{ \beta_1 r_1^{n/2} \cos \frac{n}{2} \theta_1 + \frac{h(\bar{n})}{\beta_2} r_2^{n/2} \cos \frac{n}{2} \theta_2 \right\} \tag{3}
$$

where

$$
r_m = \sqrt{x^2 + \beta_m^2 y^2}, \quad \theta_m = \tan^{-1}(\beta_m y / x), \quad m = 1, 2,
$$
$$
\beta_1 = \sqrt{1 - (c/C_L)^2}, \quad \beta_2 = \sqrt{1 - (c/C_S)^2}
$$
$$
h(n) = \begin{cases} 2\beta_1\beta_2/(1 + \beta_2^2): n \text{ odd} \\ (1 + \beta_2^2)/2: n \text{ even} \end{cases} \quad \text{and} \quad h(\bar{n}) = h(n+1)
$$
$$
C_L = \sqrt{\frac{(\kappa+1)\mu}{(\kappa-1)\rho}}, \quad C_S = \sqrt{\frac{\mu}{\rho}},
$$
$$
\kappa = \begin{cases} (3 - \nu)/(1 + \nu): \text{plane stress} \\ (3 - 4\nu): \text{plane strain} \end{cases}
$$
$$
B_I(c) = \frac{(1 + \beta_2^2)}{D}, \quad B_{II}(c) = \frac{2\beta_2}{D}, \quad D = 4\beta_1\beta_2 - (1 + \beta_2^2)^2 \tag{4}
$$

In the above, C_L is the longitudinal wave speed, C_S is the shear wave speed, c is the velocity of the crack, and x and y are the Cartesian coordinates with x aligned with the crack [28]. The crack initiation SIF ($K_{I-\text{ini}}^d$) was determined as the SIF value for the image where crack growth was first observed.

Finite Element (FE) Analysis. The use of relatively small samples, the resulting complex stress-wave reflections and the SIF
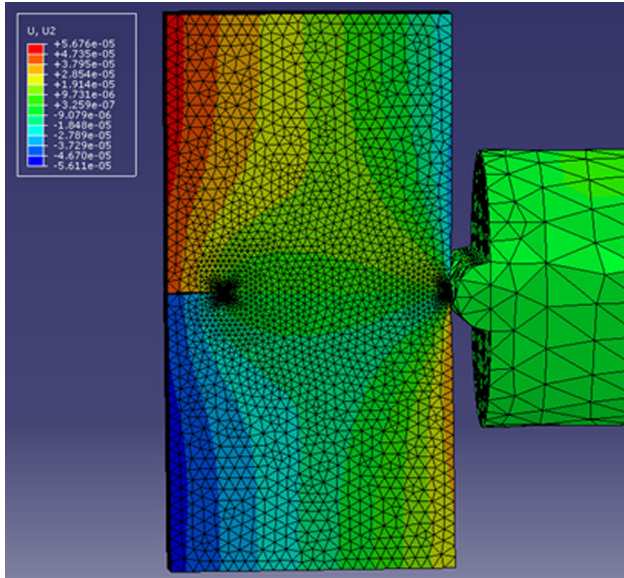
Fig. 8 Finite element model with corresponding crack opening displacement contours are shown on the specimen, along with the far left end of the long-bar. A fine mesh is used near the impact site to ensure that contact and crack tip deformation responses are captured accurately. The field corresponds to a time instant 35 μs after impact.

estimation scheme based on a few terms of the asymptotic expansion field, all demanded an independent SIF evaluation scheme to enhance the confidence level of measurements in the pre- and postinitiation regime. Accordingly, complementary finite element analyses were carried out to supplement experimental results prior to crack initiation. A 3D, transient, elastodynamic, finite element model using ABAQUS®/EXPLICIT software was developed. The model included the specimen and the long-bar (Fig. 8) in order to ensure that the stress wave propagating into the specimen was captured as accurately as possible. The model consisted of 160,000 tetrahedral elements with highly refined elements of size 0.1 mm in the impact and crack tip vicinities. The model had a total of 100,000 degrees of freedom. The particle velocity in the bar was determined from the measured strain history on the long-bar using

$$v_{pI} = c_I \varepsilon_I \tag{5}$$

and input at the far right flat surface of the long-bar (Fig. 8). After propagating along the long-bar, the stress waves were transmitted into the specimen using a contact definition for the semicircular region that impacts the flat edge of the specimen. Time increments automatically chosen during computations by the software were approximately 10 ns.

SIFs were computed from finite element results using a regression analysis of crack flank displacements. Apparent stress intensity factors ($\bar{K}_I$) were calculated using crack opening displacements (δ_y) near the crack tip according to

$$\delta_y\big|_{\theta=\pm\pi, r\to 0} = \frac{8\bar{K}_I}{E}\sqrt{\frac{r}{2\pi}} \tag{6}$$

The linear regions of $\bar{K}_I$ versus r plots were then extrapolated to the crack tip to obtain instantaneous SIFs as $K_I = \lim_{r\to 0}\bar{K}$ [29].

The various material properties used in the finite element simulation and experimental analysis are given in Table 3. Here, the elastic properties of PMMA and BC were determined ultrasonically using pulse-echo transducers.

**Table 3 Material properties used in the computational and experimental analysis**

|	PMMA	Bone cement	Al 7075 T6
E (GPa)	6.16	5.99	71.7
υ	0.32	0.31	0.30
G (GPa)	2.33	2.29	27.6
ρ (kg/m^3)	1160	1180	2730
C_L (m/s)	2430	2370	5370
C_S (m/s)	1420	1390	3180

Results

Quasi-Static Results. A pair of load versus load-point deflection responses for PMMA and bone cement specimens is shown in Fig. 9. As noted earlier, the peak load values were used in Eq. (1) for determining the quasi-static crack initiation SIF (K_{IC}). The results did not show significant difference in quasi-static crack initiation SIF between PMMA and BC. K_{IC} was found to be 1.32 ± 0.17 MPa$\sqrt{m}$ for PMMA and 1.34 ± 0.06 MPa$\sqrt{m}$ for BC. In Fig. 9, PMMA response is linear prior to crack initiation before failing catastrophically. On the other hand, BC samples show modest nonlinearity prior to initiation, and the load drop during growth is slightly more gradual.

Dynamic Results. Figure 10 shows SIF histories for PMMA and BC, along with those from FE simulations prior to crack initiation. Data from at least three test specimens for each material type are presented in these plots. Given the highly transient nature of crack growth, remarkable consistency in dynamic SIF histories is evident. In each of these graphs, solid symbols are used to denote pre- and postinitiation values whereas the values corresponding to crack initiation are denoted by enlarged open symbols.

As expected, the preinitiation slope of K_I versus t plot increases with increasing loading rate, regardless of the material being tested. This portion of the SIF histories prior to initiation closely resembles the shape of the corresponding stress-wave input from Fig. 5(a). Immediately after initiation, a dip occurs for the Al pulse shaper (medium loading rate: 10.7 strains/s) and Al/PC pulse shaper (low loading rate: 3.7 strains/s) tests, while the SIFs for the highest loading rate tests (without any pulse shaper: 42.0 strains/s) continue to increase significantly. For the remaining portion of the SIF histories, K_I^d values increase monotonically for every test type. For this region, the slopes of dynamic stress intensity factors K_I^d versus t increase significantly with increasing
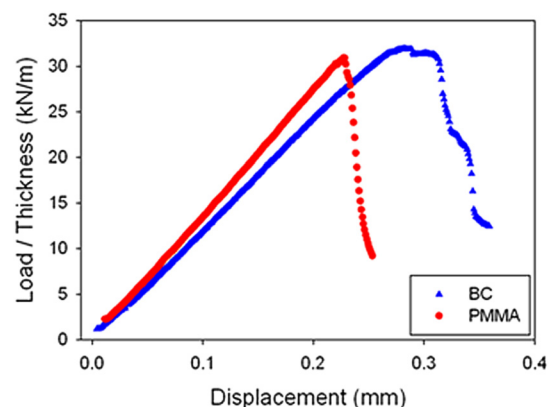
Fig. 9 Quasi-static load versus displacement curves for PMMA and bone cement. Loads have been normalized by specimen thickness. Peak loads are similar, but BC fracture is relatively less catastrophic than PMMA.
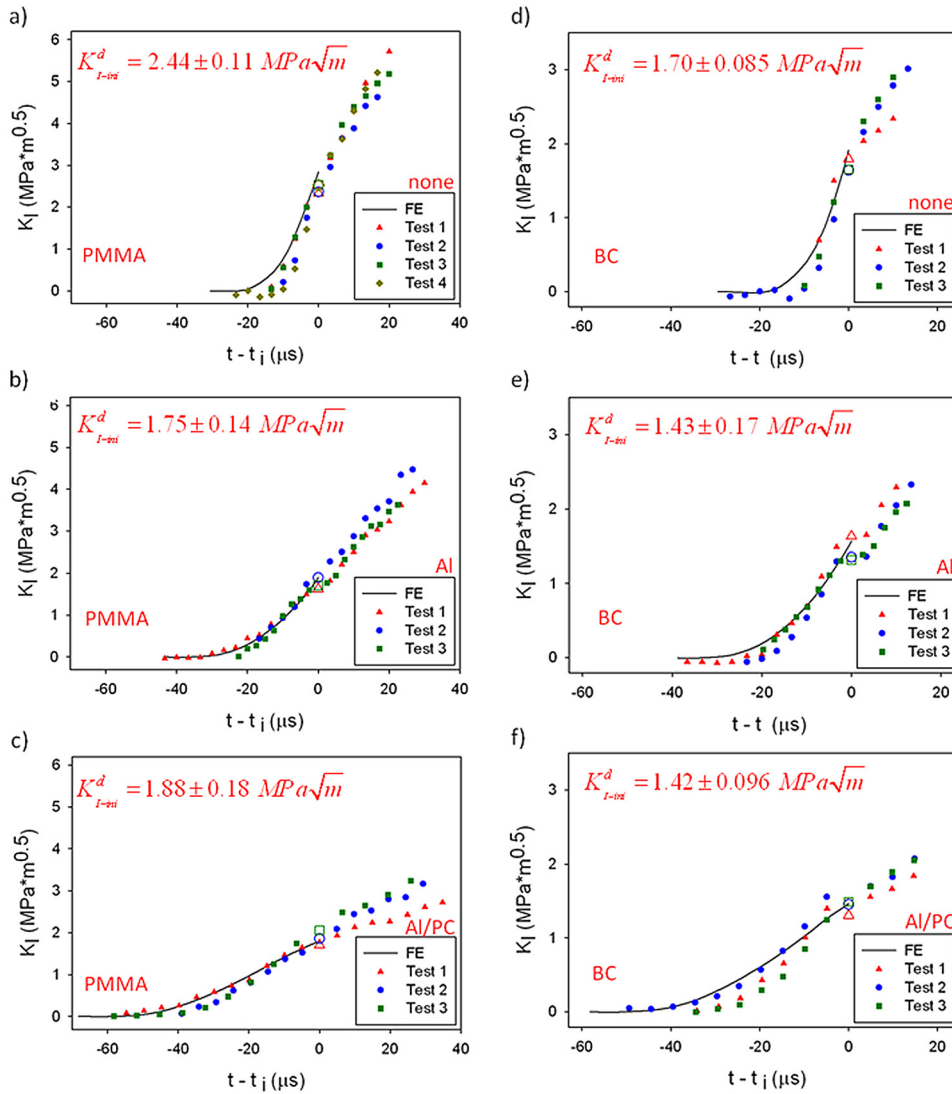
Fig. 10 SIF histories for (*a*) PMMA with no pulse shaper, (*b*) PMMA with Al pulse shaper, (*c*) PMMA with Al/PC sandwich pulse shaper, (*d*) BC with no pulse shaper, (*e*) BC with Al pulse shaper, (*f*) BC with Al/PC sandwich pulse shaper. Curves have been aligned according to time of crack initiation (t_i). (Note: The scale used is consistent for a material type but different for PMMA and BC.)

loading rate for both material types, even though there was little difference in crack initiation SIF $(K^d_{I-\text{ini}})$ between the two lower loading rate groups. In all the cases presented in Fig. 10, the finite element simulations capture the overall behavior rather well up to crack initiation. Because crack growth criteria were not included in the computational model, the numerical data were plotted up to initiation only.

It is important to note that, although tests involving the same loading rate have very similar shapes, the scales for PMMA and BC are not the same. (All tests of the same material share the same scale.) For each loading rate used, higher dynamic crack initiation SIF is seen in PMMA than the corresponding tests on BC. For both PMMA and BC, the high loading rate groups (no pulse shaper) had significantly higher $K^d_{I-\text{ini}}$ than the other two groups for the same material, although there was little difference in $K^d_{I-\text{ini}}$ between the Al and Al/PC pulse shaper cases. In order to more easily visualize these comparisons, a representative plot from each of six testing groups is given in Fig. 11.

The severity of transients results in larger error bars since they are estimated via numerical differentiation of crack length data. A combination of high loading rates and a relatively small sample
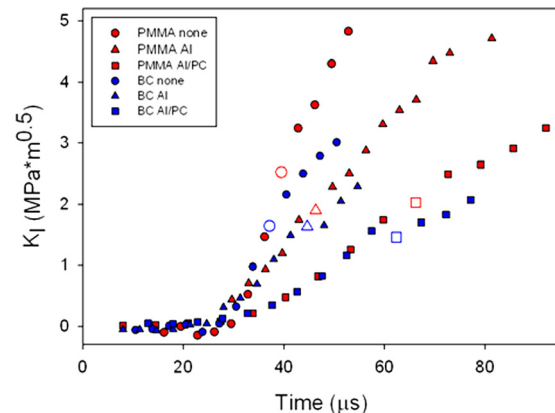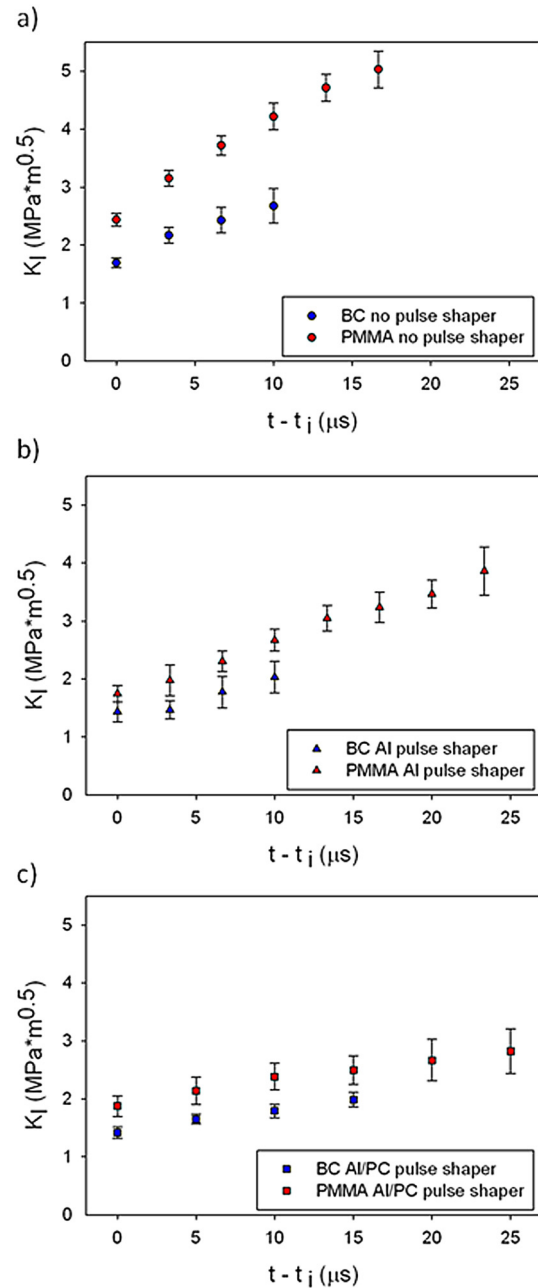

Fig. 11 Representative SIF histories from each of six testing groups from Fig. 10. Curves have been aligned according to time of impact.
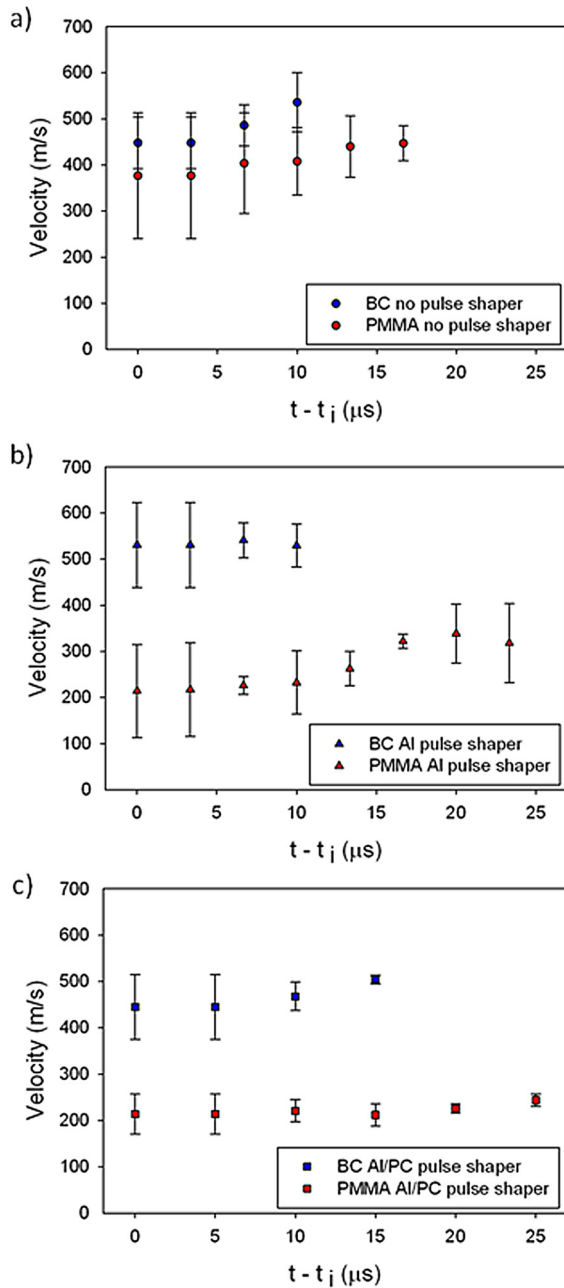
Fig. 12 The effect of material type on crack velocity is shown for (*a*) no pulse shaper (high loading rate: 42.0 s^{-1}), (*b*) Al pulse shaper (medium loading rate: 10.7 s^{-1}), and (*c*) Al/PC pulse shaper (low loading rate: 3.7 s^{-1}). $t = 0$ corresponds to crack initiation. Error bars indicate one standard deviation relative to the average value.

Fig. 13 The effect of material type on dynamic SIF is shown for (*a*) no pulse shaper (high loading rate: 42.0 s^{-1}), (*b*) Al pulse shaper (medium loading rate: 10.7 s^{-1}), and (*c*) Al/PC pulse shaper (low loading rate: 3.7 s^{-1}). $t = 0$ corresponds to crack initiation. Error bars indicate one standard deviation relative to the average value.

produces fewer data points when compared to typical drop-tower tests [26]. Within these limitations, the following observations can be made. For each loading rate, BC had significantly higher crack tip velocity than PMMA. Because BC crack tips were moving faster, the data were available for collection over a shorter duration. Further, there was little variation in crack speed for BC with loading rate; all crack tip velocities were around 500 m/s. In contrast, PMMA crack velocities generally increased with loading rate. Throughout the observation period, PMMA crack speeds were significantly higher for the highest loading rate compared to the other two rates. Both Al and Al/PC pulse shaper cases for PMMA initially have crack velocities around 200 m/s; however, velocity in the Al pulse shaper case increases steadily throughout

the test to around 300 m/s, while Al/PC pulse shaper case maintains fairly constant velocity, near 200 m/s.

Figure 13 shows combined dynamic SIF history comparison for the growing crack in PMMA and BC. For each loading rate, PMMA had significantly higher K_I^d values than BC. Again, fewer postinitiation data points are available for BC due to higher crack velocity for all loading rates. As mentioned earlier, the rate of change of K_I^d (postinitiation) increases with loading rate for both material types. For BC, the highest loading rate group had significantly higher K_I^d values than the two lower loading rate groups, and there was no significant distinction between the two lower loading rate groups. For PMMA, the same trend continued as with crack tip velocity. The highest loading rate group had significantly

Table 4   Compilation of crack initiation SIFs for PMMA and BC for each of the four loading rates

| Pulse shaper	Average $\dot{K}$ (MPa$\sqrt{\text{m}}$ s^{-1})	Average PMMA $K_{IC}/K^d_{I-\text{ini}}$ (MPa$\sqrt{\text{m}}$)	Average BC $K_{IC}/K^d_{I-\text{ini}}$ (MPa$\sqrt{\text{m}}$)
None	2.40×10^5	2.44 ± 0.11	1.70 ± 0.09
Al	0.98×10^5	1.75 ± 0.14	1.43 ± 0.17
Al/PC	0.65×10^5	1.88 ± 0.18	1.42 ± 0.10
Quasi-static	3.00×10^{-2}	1.32 ± 0.17	1.34 ± 0.06

higher K^d_I values than the other two groups throughout the entire test period, while the medium loading rate group had similar values to the lower loading rate group initially, but eventually increased to well over 3 MPa$\sqrt{\text{m}}$.

All quasi-static and dynamic crack initiation SIFs are compiled in Table 4, along with the corresponding $\dot{K}$ values representing the loading rate. The rate of change in SIF over time, $\dot{K}$, was determined experimentally for each type of pulse shaper using dynamic experimental results of PMMA just before crack initiation. All three dynamic $\dot{K}$ values are more than 6 orders of magnitude greater than the quasi-static case. All dynamic crack initiation SIF values ($K^d_{I-\text{ini}}$) are higher than the quasi-static crack initiation SIF values (K_{IC}), but the difference is much more significant for PMMA than BC.

To further examine the relative strain-rate effects on PMMA and BC, fractographic examination of failed specimens was undertaken. Micrographs of the fracture surfaces are shown in Fig. 14 for PMMA and Fig. 15 for BC. (Several optical micro-graphs were imaged and stitched to produce Fig. 14 and hence the contrast jumps along the crack growth direction periodically.) Typical mirror, mist and hackle regions were observed on PMMA fracture surfaces. Parabolic features first appear in the mist region. The pattern becomes increasingly dense with increasing resistance to crack growth until the hackle region, where parabolas overlap, indicating maximum surface roughness [30]. Because the specimen in Fig. 14(a) experiences a much higher loading rate than in Fig. 14(b), these features occur much closer to the original crack front. This trend continues in Table 5 for all three loading rates. The distance r from the original crack front to these key surface features increases with decreasing loading rate.

In contrast, microscopy of bone cement (Fig. 15) does not show these parabolic features. Instead, these images indicate that the crack bypassed prepolymerized beads. That is, fracture occurred either within the interbead matrix or along the interfaces of the two phases. Thus, both images indicate higher roughness of
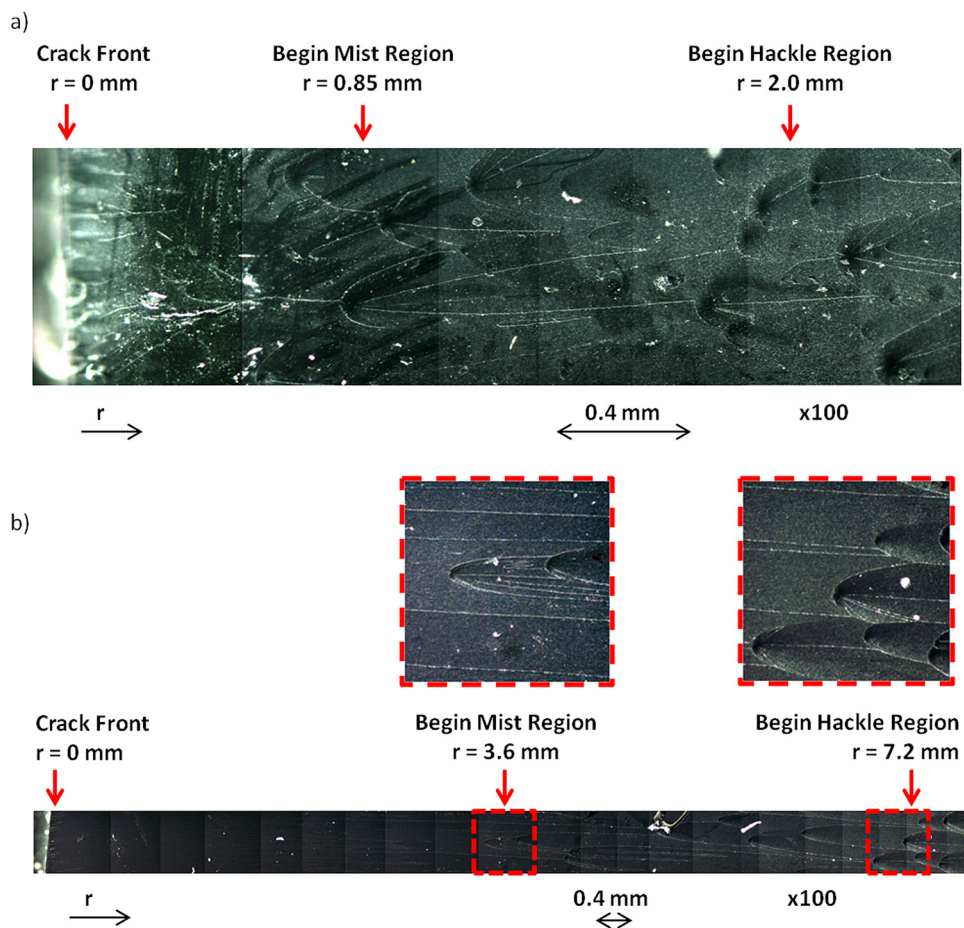
Fig. 14   Micrographs of PMMA fracture surfaces: (*a*) no pulse shaper and (*b*) Al/PC pulse shaper. Arrows indicate the beginning of common fracture surface regions. Increasing distance *r* is related to decreased resistance to crack growth.

Table 5 Distance (*r*) from the original crack front to fracture regions for each loading rate on PMMA. *r* increases with decreasing loading rate

Pulse shaper	None (mm)	Al (mm)	Al/PC (mm)
Mist	0.58	1.7	2.2
Hackle	1.2	2.9	5.5

the fracture surface than PMMA. Roughness is again higher for the higher loading rate image (Fig. 15(*a*)).

Discussion and Conclusions

A methodology to perform high-strain rate fracture tests on relatively small size specimens made of bone cement has been presented. It involves full-field measurement of displacements near a propagating crack using DIC and high-speed photography. The approach is capable of measuring pre- and postinitiation response of materials subjected to transient loading using a long-bar and gas-gun apparatus. Potential applications of the methodology include understanding dynamic fracture mechanics of cortical bone, bone cement/bone interfaces, bone cement/implant interfaces, and other materials that are difficult to obtain in traditional sizes/geometries.

Quasi-static crack initiation SIF (K_{IC}) for PMMA and bone cement (1.32 ± 0.17 and 1.34 ± 0.06 MPa$\sqrt{m}$, respectively) show good agreement with the results reported in the literature (Tables 1 and 2). Dynamic crack initiation SIF (K_I^d) for PMMA ($1.75 - 2.44$ MPa$\sqrt{m}$) measured at $\dot{K} = 6.5 - 24 \times 10^3$ MPa$\sqrt{m}$/s is also within the range of values reported from previous tests (Table 2).

Both PMMA and BC show modest loading rate dependency, but the effect is much greater for PMMA. This is evidenced by the crack initiation SIFs reported in Table 4, as well as the crack velocity and postinitiation dynamic SIF histories in Figs. 12 and 13. PMMA exhibits much greater disparity than bone cement for all these fracture data both at initiation and after initiation than bone cement. Additionally, the microscopy of PMMA shows a clear change in surface morphology with an increase in loading rate, while there is little change for bone cement with the same increase in loading rate at the same magnification. These findings are likely due to the microscopic inhomogeneity of BC, shrinkage stresses
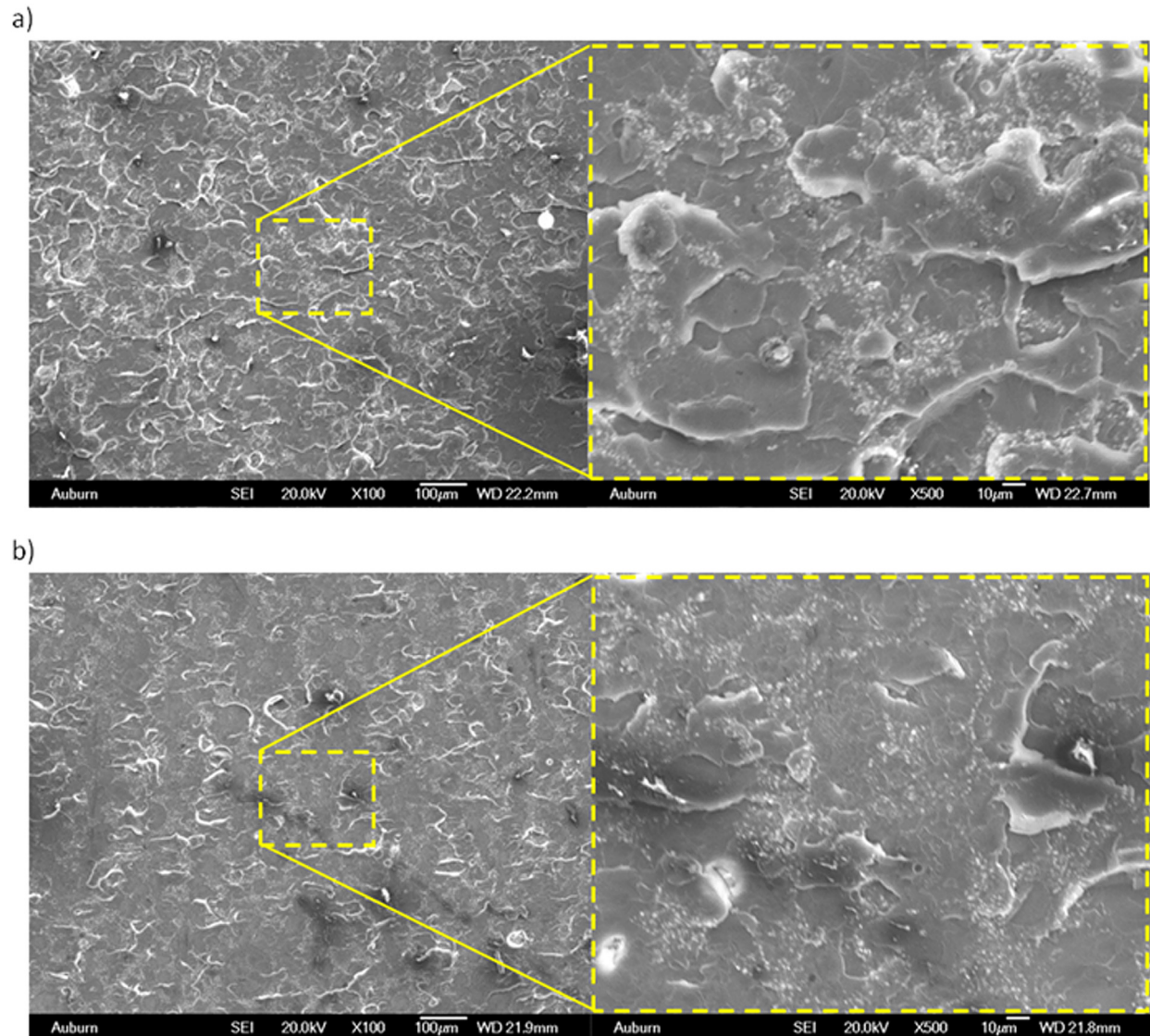
Fig. 15 Micrographs of fractured BC samples: (*a*) no pulse shaper (×100 and ×500) and (*b*) Al/PC pulse shaper (×100 and ×500). Higher roughness is shown for the higher loading rate in (*a*), and both images exhibit more roughness than PMMA (Fig. 13). Images were captured at a distance of ∼5 mm from crack front.

along the interfaces of the two phases, and the nonbonding BaSO$_4$ inclusions within the interbead matrix of BC. While these results are not particularly encouraging for the usage of cemented implants in active patients where dynamic impact events are likely, further investigation with pure PMMA (without cross-linking agent) and with various types of bone cements is warranted.

In their fatigue failure studies, Baleani and Viceconti found a 66% reduction in crack growth rate with the addition of 10% by weight BaSO$_4$ to the powder phase. They reasoned that this decrease in crack growth rate was due to cracks bypassing prepolymerized PMMA beads and instead propagating through the interbead matrix, which contained nonbonding BaSO$_4$ inclusions [10]. These BaSO$_4$ inclusions attracted the crack, turning it away from its original path. This increased the effective stress intensity factor and slowed the crack growth [10]. Similar behavior could also explain the nonlinearity of the load–deflection curve observed prior to initiation in the quasi-static tests of BC in this work, as well as the increased resistance to crack growth immediately after initiation (Fig. 9). In contrast, quasi-static load–deflection graphs for PMMA were linear until abrupt failure. However, in all of the dynamic cases, PMMA was superior in resisting crack growth (higher SIFs and lower crack velocities) despite much lower roughness than BC. This suggests that either the two phases of the BC were weakly bonded and allowed prepolymerized beads to pull out of the interbead matrix, or the BaSO$_4$ nonbonding inclusions greatly weakened the interbead matrix and caused the crack to follow the interbead matrix at relatively high speeds.

Further research is necessary in order to improve the dynamic fracture characteristics of bone cement. Possible solutions include improving the bonding between radiopacifier and interbead matrix, and reducing shrinkage stresses between interbead matrix and prepolymerized beads.

Acknowledgment

References

[1] Charnley, J., 1960, "Anchorage of the Femoral Head Prosthesis to the Shaft of the Femur," J. Bone Jt. Surg., Br. Vol., **42**(1), pp. 28–30.

[2] Stanczyk, M., 2005, "Study on Modelling of PMMA Bone Cement Polymerisation," J. Biomech., **38**(7), pp. 1397–1403.

[3] Lewis, G., 1999, "Effect of Mixing Method and Storage Temperature of Cement Constituents on the Fatigue and Porosity of Acrylic Bone Cement," J. Biomed. Mater. Res., **48**(2), pp. 143–149.

[4] Ramakrishna, S., Mayer, J., Wintermantel, E., and Leong, K. W., 2001, "Biomedical Applications of Polymer-Composite Materials: A Review," Compos. Sci. Technol., **61**(9), pp. 1189–1224.

[5] Chu, K. T., Oshida, Y., Hancock, E. B., Kowolik, M. J., Barco, T., and Zunt, S. L., 2004, "Hydroxyapatite/PMMA Composites as Bone Cements," Biomed. Mater. Eng., **14**(1), pp. 87–105.

[6] Jasty, M., Maloney, W. J., Bragdon, C. R., Oconnor, D. O., Haire, T., and Harris, W. H., 1991, "The Initiation of Failure in Cemented Femoral Components of Hip Arthroplasties," J. Bone Jt. Surg., Br. Vol., **73**(4), pp. 551–558.

[7] Topoleski, L. D. T., Ducheyne, P., and Cuckler, J. M., 1990, "A Fractographic Analysis of *In Vivo* Poly(methyl methacrylate) Bone Cement Failure Mechanisms," J. Biomed. Mater. Res., **24**(2), pp. 135–154.

[8] Jasty, M., Davies, J. P., Oconnor, D. O., Burke, D. W., Harrigan, T. P., and Harris, W. H., 1990, "Porosity of Various Preparations of Acrylic Bone Cements," Clin. Orthop. and Relat. Res., **259**, pp. 122–129.

[9] Buckley, P. J., Orr, J. F., Revie, I. C., Breusch, S. J., and Dunne, N. J., 2003, "Fracture Characteristics of Acrylic Bone Cement-Bone Composites," Proc. Inst. Mech. Eng., Part H: J. Eng. Med., **217**(H6), pp. 419–427.

[10] Ishihara, S., Goshima, T., Kanekasu, K., and McEvily, A. J., 2002, "The Static and Cyclic Strength of a Bone-Cement Bond," J. Mater. Sci. Mater. Med., **13**(5), pp. 449–455.

[11] Vallo, C. I., Cuadrado, T. R., and Frontini, P. M., 1997, "Mechanical and Fracture Behaviour Evaluation of Commercial Acrylic Bone Cements," Polym. Int., **43**(3), pp. 260–268.

[12] Baleani, M., and Viceconti, M., 2011, "The Effect of Adding 10% of Barium Sulphate Radiopacifier on the Mechanical Behaviour of Acrylic Bone Cement," Fatigue Fract. Eng. Mater. Struct., **34**(5), pp. 374–382.

[13] Johnson, J. A., and Jones, D. W., 1994, "The Mechanical Properties of PMMA and Its Copolymers With Ethyl Methacrylate and Butyl Methacrylate," J. Mater. Sci., **29**(4), pp. 870–876.

[14] Rittel, D., and Maigre, H., 1996, "An Investigation of Dynamic Crack Initiation in PMMA," Mech. Mater., **23**(3), pp. 229–239.

[15] Weerasooriya, T., Moy, P., and Casem D., 2006, "Fracture Toughness for PMMA as a Function of Loading Rate," Proceedings of the 2006 SEM Annual Conference and Exposition on Experimental and Applied Mechanics, St. Louis, MO, June 4–7.

[16] Wada, H., 1992, "Determination of Dynamic Fracture-Toughness for PMMA," Eng. Fract. Mech., **41**(6), pp. 821–831.

[17] Wada, H., Seika, M., Calder, C. A., and Kennedy, T. C., 1993, "Measurement of Impact Fracture Toughness for PMMA With Single-Point Bending Test Using an Air Gun," Eng. Fract. Mech., **46**(4), pp. 715–719.

[18] Nam, H. W., Aggag, G. A., Takahashi, K., and Han, K. S., 2000, "The Dynamic Behavior of Metal-Matrix Composites Under Low-Velocity Impact," Compos. Sci. Technol., **60**(6), pp. 817–823.

[19] Martins, C. E., Irfan, M. A., and Prakash, V., 2007, "Dynamic Fracture of Linear Medium Density Polyethylene Under Impact Loading Conditions," Mater. Sci. Eng., A, **465**(1-2), pp. 211–222.

[20] Weisbrod, G., and Rittel, D., 2000, "A Method for Dynamic Fracture Toughness Determination Using Short Beams," Int. J. Fract., **104**(1), pp. 89–103.

[21] Dai, F., Chen, R., Iqbal, M. J., and Xia, K., 2010, "Dynamic Cracked Chevron Notched Brazilian Disc Method for Measuring Rock Fracture Parameters," Int. J. Rock Mech. Min. Sci., **47**(4), pp. 606–613.

[22] Dong, S. M., Wang, Y., and Xia, Y. M., 2006, "A Finite Element Analysis for Using Brazilian Disk in Split Hopkinson Pressure Bar to Investigate Dynamic Fracture Behavior of Brittle Polymer Materials," Polym. Test., **25**(7), pp. 943–952.

[23] Dai, F., Chen, R., and Xia, K., 2010, "A Semi-Circular Bend Technique for Determining Dynamic Fracture Toughness," Exp. Mech., **50**(6), pp. 783–791.

[24] Wang, Q. Z., Feng, F., Ni, M., and Gou, X. P., 2011, "Measurement of Mode I and Mode II Rock Dynamic Fracture Toughness With Cracked Straight Through Flattened Brazilian Disc Impacted by Split Hopkinson Pressure Bar," Eng. Fract. Mech., **78**(12), pp. 2455–2469.

[25] Shukla, A., Parameswaran, V., Du, Y., and Evora, V., 2006, "Dynamic Crack Initiation and Propagation in Nanocomposite Materials," Rev. Adv. Mater. Sci., **13**(1), pp. 47–58.

[26] Lee, D., Tippur, H., Kirugulige, M., and Bogert, P., 2009, "Experimental Study of Dynamic Crack Growth in Unidirectional Graphite/Epoxy Composites Using Digital Image Correlation Method and High-Speed Photography," J. Compos. Mater., **43**(19), pp. 2081–2108.

[27] Baleani, M., Cristofolini, L., Minari, C., and Toni, A., 2003, "Fatigue Strength of PMMA Bone Cement Mixed With Gentamicin and Barium Sulphate vs Pure PMMA," Proc. Inst. Mech. Eng., Part H: J. Eng. Med., **217**(H1), pp. 9–12.

[28] Nishioka, T., and Atluri, S. N., 1983, "Path Independent Integrals, Energy Release Rates, and General Solutions of Near-Tip Fields in Mixed-Mode Dynamic Fracture Mechanics," Eng. Fract. Mech., **18**(1), pp. 1–22.

[29] Rousseau, C. E., and Tippur, H. V., 2001, "Influence of Elastic Gradient Profiles on Dynamically Loaded Functionally Graded Materials: Cracks Along the Gradient," Int. J. Solids Struct., **38**(44-45), pp. 7839–7856.

[30] Plangsangmas, L., Mecholsky, J. J., and Brennan, A. B., 1999, "Determination of Fracture Toughness of Epoxy Using Fractography," J. Appl. Polym. Sci., **72**(2), pp. 257–268.